A Fast Calculation Method of Electromagnetic Performance of Skewed Eccentric Brushless DC Motor

Li Wang[*]

Henan Key Laboratory of Optoelectronic Sensing Integrated Application, College of Electronic and Electrical Engineering, Henan Normal University, Xinxiang 453007, China
*Corresponding Author.

Abstract:

This paper investigates a fast calculation method for electromagnetic performance, including back electromotive force (EMF), cogging torque, and electromagnetic torque, of brushless DC motor (BLDCM) with skewed stator core and static rotor eccentricity. The idea of the algorithm is that the whole eccentric skewed motor is divided into several equal-thickness slices along the axial direction, and the straight slot motors are used instead of these slices to participate in the performance calculation. 2-D finite element (FE) method is adopted to calculate these straight slot motors, and the calculated results are superimposed according to the designed rules. The selection rule of slice number is discussed in detail, and the electromagnetic performance of healthy motor and eccentric motor is compared. Compared with the 3-D FE method, this method can greatly reduce the calculation amount and shorten the solution time. Experimental results show the effectiveness of the algorithm. The research results can provide reference for performance calculation of skewed eccentric BLDCM.

Keywords: Brushless DC Motor, skew, electromagnetic performance.

I. INTRODUCTION

BLDCM is a typical mechatronics product. Because of its advantages such as large starting torque, strong overload capacity, long service life, reliable operation and high efficiency, it is widely used in CNC machine tools, electric vehicles, aviation, national defense and other fields[1-5]. However, when the machining accuracy is low, or the assembly is poor, or the parts are worn after long-term work, it will inevitably cause different degrees of eccentricities.

Eccentricities will obviously change the magnetic field distribution inside the motor, and then affect the electromagnetic performance of the motor. In the current literatures, many scholars have done extensive research on various types of eccentricity. [6] proposes an equivalent air-gap length model for interior permanent magnet motor by the magnetic potentials of inner stator surface and outer rotor surface, and the winding inductances under diverse stator currents and rotor eccentricity are solved. [7] proposes a

new complex analytical model to reveal the single sideband modulation effect caused by dynamic eccentricity in the air-gap magnetic field , and a diagnostic method is designed to identify the type and degree of eccentricity. [8] discusses the influence of dynamic and static eccentricity on electromagnetic force in different structures of permanent magnet synchronous motors. [9] presents an analytical method for predicting the magnetic field in surface-mounted PM synchronous motor with rotor eccentricity using hybrid magnetic circuit and subdomain method. [10] studies the influences of different types of rotor eccentricities on air gap flux density, EMF, electromagnetic torque, cogging torque and UMF in 2-pole /3-slot PM motors. [11] proposes a method for detecting and classifying various faults including dynamic eccentricity by detecting the voltage of an air gap search coil. [12] presents a rotor inter-turn short circuit fault analysis model of synchronous generator considering static air-gap eccentricity. [13] analyses and tests the electromechanical characteristics of PM synchronous motor, which is mainly used in industrial power tools. [14] presents a method of online detection and identification of magnetic field winding insulation and rotor eccentricity faults in synchronous generators based on the measured value of air-gap flux probe. [15] improves the dynamic model of bearingless asynchronous motor considering load change and rotor eccentricity. [16] presents an online fault detection method, which can detect two kinds of faults including air-gap eccentricity, of synchronous generator based on residual analysis.

According to research content, the literatures on eccentricities can be divided into the following two categories: (i) Type of eccentric fault is diagnosed accurately and nondestructive by detecting characteristic signals such as current, voltage or magnetic field; (ii) Operation characteristics of the motor are predicted under various eccentric faults. This paper belongs to the latter.

The traditional magnetic circuit method is often used to calculate normal motors with traditional topology in engineering, which has high speed and acceptable accuracy. However, its simplified mathematical model cannot consider subtle magnetic circuit changes. The FE model has high calculation accuracy and can reflect any detail changes of the magnetic circuit, but its calculation amount is much larger than that of the magnetic circuit method. The skew is an effective way to restrain torque ripple, which is widely used in designing PM motors. Because of the particularity of mechanical structure, it is often necessary to establish a 3-D FE model to analyze the skewed motor. Considering the huge amount of calculation of the 3-D FE model, the simplified modeling idea of multi-slice is often adopted for the skewed motor. There are already many researches on eccentricities of straight slot motors, but few on the skewed. In this paper, the multi-slice model is used to study the eccentric skewed motor.

In some literatures, after solving the motor units of the multi-slice model, it is necessary to solve the field-circuit coupling equations to synthesize the results of the whole skewed motor from 2-D field analysis data sequences, which is very complicated[17-23]. In order to solve this problem, different from the circuit model driven by constant voltage source which is usually used in ordinary FE modeling, an equivalent algorithm is proposed which adopts constant current source circuit to make the conductor currents in the same slot of motor units equal. In this paper, the equivalent algorithm is adopted to predict the characteristics of the surface mounted PM motors driven by square wave currents with static rotor eccentricity and skewed stator slots. It does not need to solve the field-circuit coupling equation, but adopts

the way of directly superimposing data, which is very suitable for practical engineering. The relative error of the equivalent algorithm is studied theoretically and deduced. The experimental results of the prototypes prove the effectiveness of the proposed equivalent algorithm.

II. MENTALITY AND CALCULATION ACCURACY OF MULTI-SLICE MODEL

The rotor eccentricities can be divided into two basic situations: static eccentricity and dynamic eccentricity. Other eccentricity types are different combinations of these two situations. The geometric schematic diagram of rotor eccentricity is shown in Fig. 1. In order to highlight the visual effect of rotor eccentricity, the rotor size is reduced, while the air-gap thickness and eccentric distance are exaggerated. In the figure, Os is the geometric center of stator; Or is the geometric center of rotor; α is the eccentric angle of rotor; θ is the rotor position angle; e is the eccentric distance; g is the air-gap length; Rin is the inner radius of stator; rout is the outer radius of rotor; XsYs is the coordinate system of stator with Os as the origin; XRYR is the coordinate system of rotor with OR as the origin.
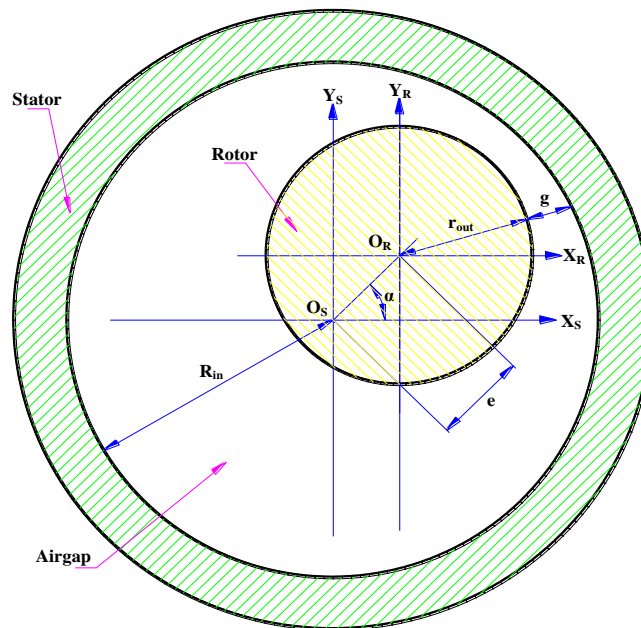

Fig. 1: Geometric schematic diagram of eccentricity fault

The rotor rotates around its own geometric center under ideal health conditions and the geometric centers of stator and rotor coincide completely. When the rotor is eccentric, the geometric centers no longer coincide. If dynamic eccentricity occurs, the rotor rotates around the stator geometric center, and the air-gap length at a certain rotor position will change due to the rotor rotation at different moments. If static eccentricity occurs, the rotor rotates around its own geometric center, and the air-gap length will not change at any time. This paper focuses on static eccentricity and the air-gap length can be expressed as

$$g = \sqrt{R_{in}^2 - e^2 \sin^2(\theta - \alpha)} - r_{out} - e\cos(\theta - \alpha) \tag{1}$$

It can be seen from (1) that the length of the air gap along the circumference is no longer equal everywhere. Considering that the magnetic permeability of air in the magnetic flux path is far less than that of iron core material, the magnetic density in the air gap will decrease as the air gap becomes thicker and increase as the air gap becomes thinner. Rotor eccentricity can be defined as

$$\kappa = \frac{e}{g_0} \times 100\% = \frac{e}{R_{in} - r_{out}} \times 100\% \tag{2}$$

where g_0 is the uniform air-gap length under the condition of complete health.

In traditional electric motor design, the magnetic circuit method is adopted normally to predict the performance of skewed motor, yet the calculation accuracy is comparatively low. In order to obtain higher calculation accuracy, the FEM is adopted frequently. The 2-D FEM has the advantages of easy modeling and less computation, and is suitable for analyzing straight slot motors whose cross sections do not change along the axial direction. The 3-D geometric structure of skewed motors will lead to the differences of axial cross sections and the 2-D FEM can not be adopted directly. Therefore, 3-D FEM has to be used to model the skewed motors. Compared with the 2-D FE model, the 3-D FE model is not only time-consuming and complex in modeling process, but also has a huge number of 3-D subdivision elements which will result in a huge amount of calculation.

In order to give consideration to both model solving time and calculation accuracy, a multi-slice equivalent algorithm is adopted to model the skewed motors. As shown in Fig. 2, the ideology of the algorithm is to divide a skewed motor into several sections along the axial direction and each of these sections is replaced with one straight slot motor unit. The thick blue diagonal line indicates the actual conductor in skewed stator slot, while the thick red segmented vertical thick lines represent the equivalent conductors of motor units. The 2-D FEM can be adopted to model the straight slot motor unit and the performances of the whole skewed motor are obtained by numerically processing the 2-D FEM calculated data sequences according to the designed rules. The model established by the equivalent algorithm can meet the precision needs of general engineering, and also has a short time to solve. In the figure, n is the number of slices, β is the skew angle of skewed motor, β/n is the skew angle of one motor unit, L is the projection length of winding conductor along the axial direction of motor, L/n is the projection length of one motor unit.
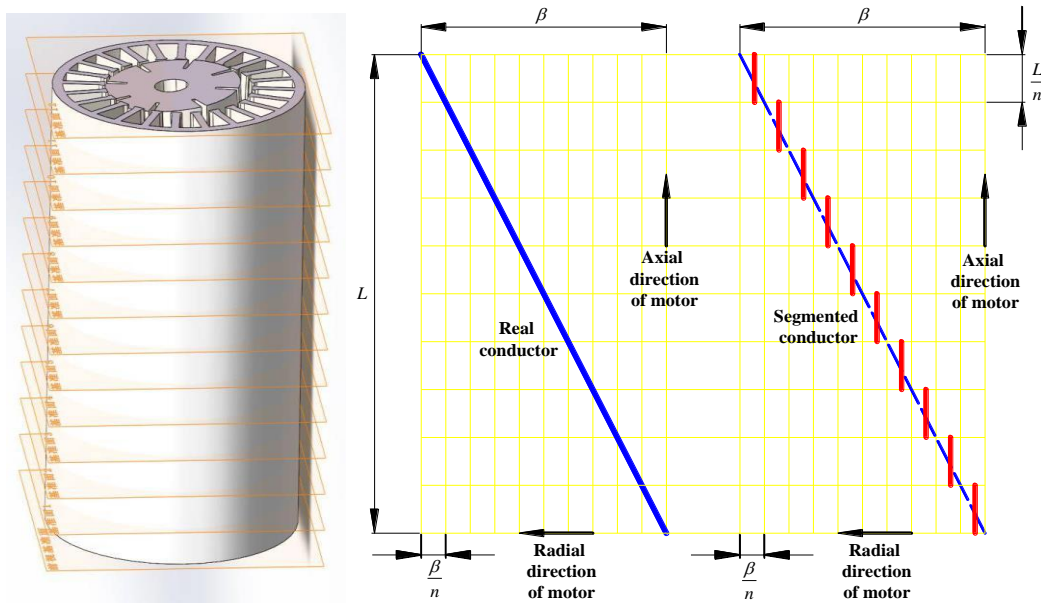
Fig. 2: Ideology of equivalent algorithm

The multi-slice model inherits the inherent shortcomings of 2-D FEM, which cannot consider the end magnetic field of motor. The equivalent algorithm adopts the ideology that a number of straight slot motor units in series are equivalent to the whole skewed motor, and its mathematical description is

$$
\begin{cases}
\nabla \times (v \nabla \times A_{zi}) + \sigma \dfrac{\partial A_{zi}}{\partial t} = J_z \\
E = \sum_{i=1}^{n} E_i = \sum_{i=1}^{n} \dfrac{d\phi_i}{dt} \\
F = \sum_{i=1}^{n} F_i
\end{cases}
\tag{3}
$$

where v is the velocity of winding coil, A_{zi} is the magnetic vector potential of motor unit, J_z is the current density, E is the EMF of winding coil, E_i is the EMF of motor unit, φ_i is the flux linkage of motor unit, F is electromagnetic force, F_i is electromagnetic force of motor unit.

In the fundamental magnetic field, the cross-sectional position of multi-slice model is schematically shown in Fig. 3.
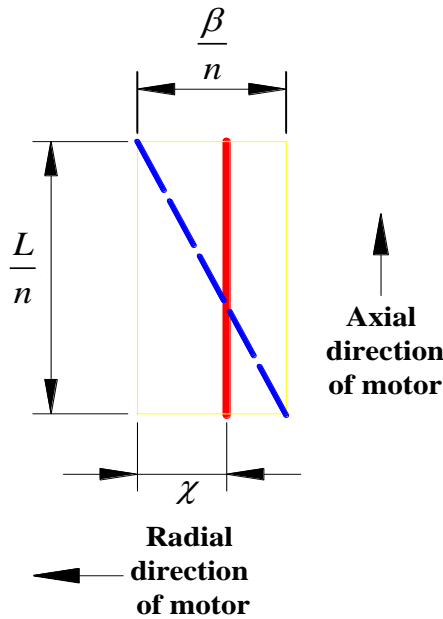
Fig. 3: Cross-sectional position of motor unit

The skew angle of motor unit can be expressed as

$$\kappa_i = \alpha + \frac{i-1}{n}\beta + \chi \tag{4}$$

Where χ is the mechanical angle between the cross-sectional position and the end point of the inclined conductor section, α is the end position of conductor section.

The electromagnetic force on current-carrying conductor in harmonic magnetic field can be expressed as

$$
\begin{cases}
F_k = \int_{\alpha_k}^{\alpha_k+\beta_k}(B_{mk}\sin\theta)I\frac{L}{\beta_k}d\theta = \frac{2}{\beta_k}B_{mk}IL\sin(\alpha_k+\frac{\beta_k}{2})\sin\frac{\beta_k}{2} = \frac{2}{k\beta}B_{mk}IL\sin(\alpha_k+\frac{k\beta}{2})\sin\frac{k\beta}{2} \\[4mm]
F_{km} = \frac{1}{n}\sum_{i=1}^{n}F_{kmi}^{'} = \frac{1}{n}\sum_{i=1}^{n}B_{mk}IL\sin[\alpha_k+(i-1)\frac{\beta_k}{n}+\chi_k] = B_{mk}IL\frac{\sin[(\alpha_k+\frac{k\beta}{2})+(k\chi-\frac{k\beta}{2n})]\sin\frac{k\beta}{2}}{n\sin\frac{k\beta}{2n}}
\end{cases}
\tag{5}
$$

where F_k is the actual electromagnetic force calculated by integral algorithm, α_k is the end position of conductor section in the harmonic magnetic field, β_k is the electrical skew angle in the harmonic magnetic field, I is the winding current, B_{mk} is the amplitude of harmonic magnetic field, k is the order of harmonic magnetic field, F_{km} is equivalent the electromagnetic force calculated by summation algorithm of multi-slice model, F_{kmi} is the electromagnetic force of motor unit, χ_k is the electrical angle between the

cross-sectional position and the end point of the equivalent inclined conductor section in harmonic magnetic field.

Based on the analogical algorithm of electromagnetic force, the EMF generated by moving conductor in harmonic magnetic field can be expressed as

$$
\begin{cases}
E_k = \int_{\alpha_k}^{\alpha_k + \beta_k} (B_{mk} \sin\theta)v \dfrac{L}{\beta_k} d\theta = \dfrac{2}{\beta_k} B_{mk} Lv \sin(\alpha_k + \dfrac{\beta_k}{2}) \sin\dfrac{\beta_k}{2} = \dfrac{2}{k\beta} B_{mk} Lv \sin(\alpha_k + \dfrac{k\beta}{2}) \sin\dfrac{k\beta}{2} \\[4mm]
E_{km} = \dfrac{1}{n}\sum_{i=1}^{n} E_{kmi} = \dfrac{1}{n}\sum_{i=1}^{n} B_{mk} Lv \sin[\alpha_k + (i-1)\dfrac{\beta_k}{n} + \chi_k] = B_{mk} Lv \dfrac{\sin(\alpha_k + \dfrac{k\beta}{2})\sin\dfrac{nk\beta}{2(n-1)}}{n\sin\dfrac{k\beta}{2(n-1)}}
\end{cases}
\tag{6}
$$

where E_k is the actual EMF calculated by integral algorithm, E_{km} is the equivalent EMF calculated by summation algorithm of multi-slice model, E_{kmi} is the EMF of motor unit.

If the influences of end region magnetic field are neglected, the relative errors of electromagnetic force and EMF calculated by multi-slice model can be expressed as

$$
\begin{cases}
\varepsilon_{Fk} = \dfrac{F_{km} - F_k}{F_k} \times 100\% = \dfrac{k\beta \sin[(\alpha_k + \dfrac{k\beta}{2}) + k(\chi - \dfrac{\beta}{2n})]}{2n\sin(\alpha_k + \dfrac{k\beta}{2})\sin\dfrac{k\beta}{2n}} - 1 \\[6mm]
\varepsilon_{Ek} = \dfrac{E_{km} - E_k}{E_k} \times 100\% = \dfrac{k\beta \sin[(\alpha_k + \dfrac{k\beta}{2}) + k(\chi - \dfrac{\beta}{2n})]}{2n\sin(\alpha_k + \dfrac{k\beta}{2})\sin\dfrac{k\beta}{2n}} - 1
\end{cases}
\tag{7}
$$

It can be seen from (7) that the relative error expressions of electromagnetic force and EMF are completely consistent. These two errors can be represented by a unified symbol, and there is no need to distinguish them in the following contents. In a certain order of harmonic magnetic field, the relative error depends not only on the number of slices, skew angle, harmonic order, but also on the cross-sectional position, the end position of the conductor section and other variables.

If and only if the cross-sectional position is taken at the midpoint of each inclined conductor section, the relative error is only related to skew angle, harmonic order and the number of slices. Then, the expression of the relative error can be simplified as

$$
\varepsilon_k = \frac{k\beta/(2n)}{\sin[k\beta/(2n)]}
\tag{8}
$$

III. SIMPLIFIED EQUIVALENT MODEL OF A SKEWED PROTOTYPE

Before establishing the simplified equivalent model of the prototype in this paper, it is necessary to analyze the influencing factors of calculation accuracy, and then select the number of slices judiciously. The skew angle of prototype is fixed at a mechanical angle of 15 degrees. The number of slices is 2 to 30 in turn, and the harmonic order is 1 to 24 in turn. The relative errors of the simplified equivalent model under different combinations are shown in Fig. 4.
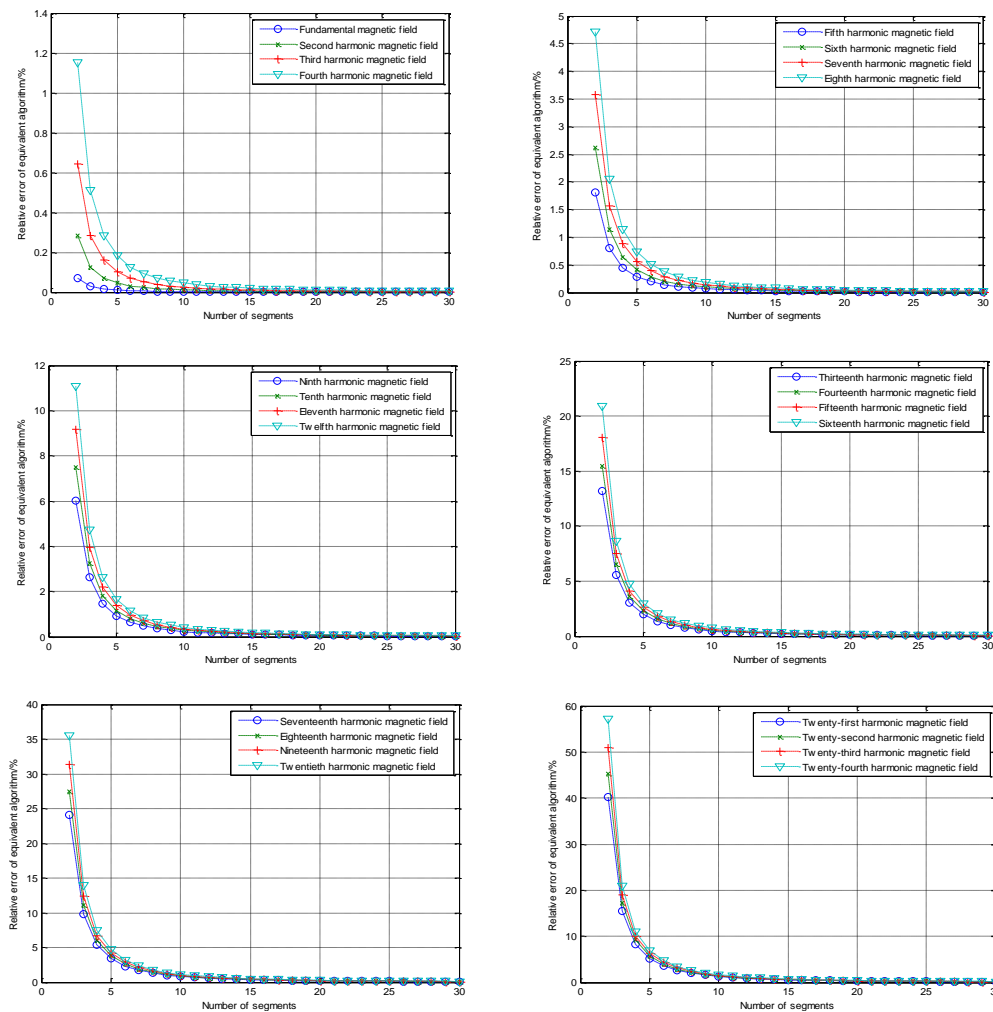
Fig. 4: Relative error of simplified equivalent model

The change trend of relative error data series is comparatively studied and the following conclusions can be drawn. If the number of slices increases, the calculation accuracy can be improved significantly in any order of harmonic magnetic field. If the number of slices is fixed, the calculation accuracy in higher order harmonic magnetic field is obviously lower than that of lower order harmonic magnetic field. Considering that the amplitude of the harmonic component of the magnetic field in the air gap of the motor

decreases significantly with the increase of harmonic order, and the amplitude of the harmonic magnetic field of higher order is extremely small, 20 is finally selected as the slice number.

The relative positions of stator and rotor of motor units in series are different at any moment, so the switch conduction intervals of different motor units are also different. Two segmentation methods, odd-numbered slices and even-numbered slices, are described respectively. The setting description of switch conduction intervals are shown in Fig. 5. In the figure, ρ_x indicates the offset angle of the switch conduction interval of the *xth* motor unit based on the optimal conduction interval of the whole skewed motor. If ρ_x takes a negative value, it means that the switches need to be turned on in advance, while a positive value means that the switches needs to be turned on late.
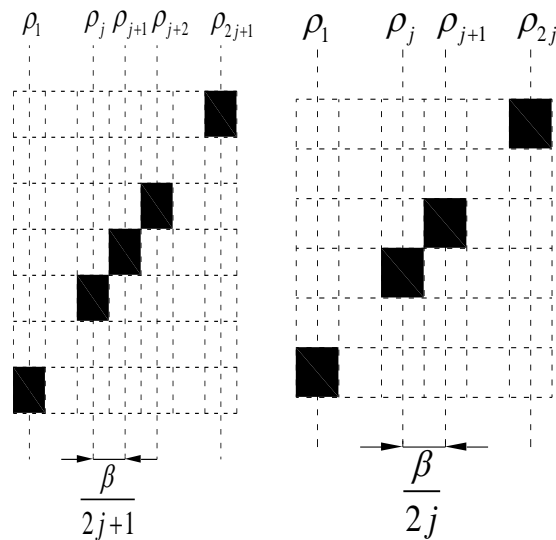
(a) odd-numbered slices   (b) even-numbered slices
Fig. 5: Setting description of switch conduction interval

If the number of slices is odd, the deviation angle of switch conduction intervals of two adjacent motor units is $\beta/(2j+1)$. The phase of EMF of the middle motor unit is the same as that of the whole skewed motor. Then, the switch conduction interval of the $(j+1)th$ motor unit is the same as that of the whole skewed motor, i.e., ρ_{j+1} takes 0. The remaining $2j$ motor units are respectively arranged on both sides of the $(j+1)th$ motor unit. On the basis of the whole skewed motor, the switch conduction intervals of the first j motor units are advanced in turn, while the switch conduction intervals of the latter j motor units are delayed in turn. The offset angle of switch conduction interval of the *ith* motor unit can be expressed as

$$\rho_i = \begin{cases} -\dfrac{\beta}{2j+1}(j-i+1) & i = 1,\cdots j \\[2mm] 0 & i = j+1 \\[2mm] \dfrac{\beta}{2j+1}(i-j-1) & i = j+2,\cdots 2j+1 \end{cases} \tag{9}$$

If the number of slices is even, the deviation angle of switch conduction intervals of two adjacent segment motor units is *β/2j*. The middle value of EMF phase of the middle two motor units is the same as that of the whole skewed motor. Compared with the whole skewed motor, the switch conduction intervals of the first *j* motor units are advanced in turn, and the switch conduction intervals of the latter *j* motor units are delayed in turn. The offset angle of switch conduction interval of the *ith* motor unit can be expressed as

$$\rho_i = \begin{cases} \dfrac{\beta}{4j} - \dfrac{\beta}{2j}(j-i+1) & i = 1,\cdots j \\[2mm] \dfrac{\beta}{4j} + \dfrac{\beta}{2j}(i-j-1) & i = j+1,\cdots 2j \end{cases} \tag{10}$$

Theoretically speaking, there are no advantages and disadvantages between odd-numbered slices and even-numbered slices. However, when setting the switch conduction intervals in modeling process, truncation errors should be avoided as much as possible. In the actual calculation process, one of the advantages of even-numbered segmentation is that the denominator in the expression of offset angle is *4j*, while the denominator in the expression of offset angle in odd-numbered segmentation is *2j+1*. In contrast, if even-numbered segmentation is adopted, the value range of variable *j* is obviously wider.

The radial cross-section of prototype is shown in Fig. 6. In the figure, A, B and C represent three phase winding areas, N and S represent different magnetization directions of PMs. The prototype has twenty-four stator slots, and each phase winding consists of four winding elements connected in series. Phase A is taken as an example and the other two phases have similar structures. A1, A2, A3 and A4 are connected in series in turn to form A-phase winding. Generally, the circuits coupled with the geometry research domain are driven by ideal voltage source in FE simulation. However, in the multi-slice model of this paper, the currents passing through the corresponding slot conductors of different motor units are exactly the same, while the voltages are different. Therefore, the simulation model of motor unit in this paper can only adopt the simulation circuit driven by constant current source, as shown in Figure 7.
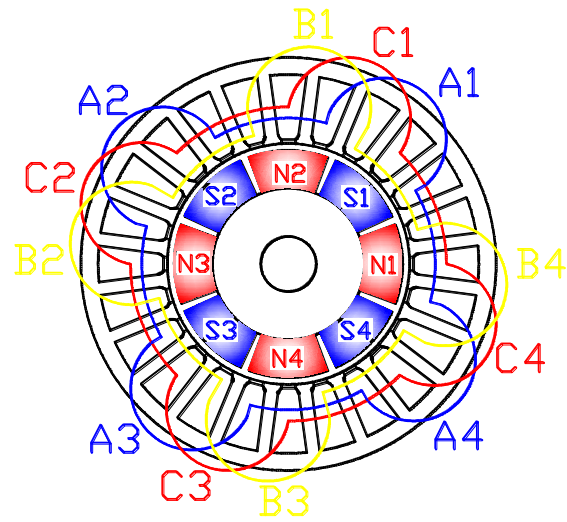
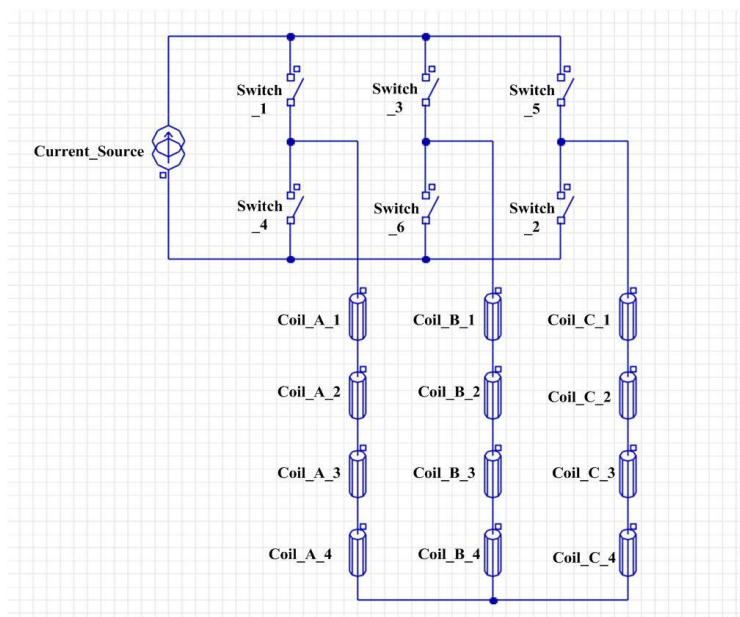Fig. 6: Radial cross-sections of stator and rotor

Fig. 7: Simulation circuit driven by constant current source

Under ideal health conditions, the air gap thickness of prototype should be 0.5 mm and equal everywhere along the circumferential direction. However, if static eccentricity occurs, rotor geometric center will deviate from stator geometric center by a certain distance. In this paper, the rotor is moved horizontally to the right by 0.2 mm, and the eccentricity reaches 0.4. Taking the new rotor geometric center as rotation center, a static eccentricity is manufactured artificially. The 2-D FE models of prototype with and without eccentricity are established respectively.

IV. CALCULATION OF PROTOTYPE

When the rotor is static eccentric, the air-gap thickness at the position of 0° circumferential position is the smallest, which is only 0.3mm, while the largest at the position of 180°, which is 0.7mm. However, the air-gap thicknesses at the position of 90° and 270° have little change. On a closed path near the center of air gap, the data sequences of normal magnetic density are shown in Fig. 8(a). As shown in the figure, the magnetic density will increase where the thickness reduces and decrease where thickens. Near N1 of the first pair of magnets, the thickness decreases the most and the magnetic density increases the most. Near N3 of the third pair, the thickness increases the most and the magnetic density decreases the most. In the vicinities of N2 of the second pair and N4 of the fourth pair, the change of magnetic density is not obvious.

The tangential magnetic density affects the radial magnetic pull of motor significantly and its data sequences are shown in Fig. 8(b). When the motor is completely healthy, the distribution of tangential magnetic density should take two polar distances as a complete cycle. However, after the occurrence of static eccentricity, the periodicity of distribution changes obviously. The resultant radial magnetic pull force will no longer be zero, which will result in unbalanced magnetic pull force acting on the motor rotor, and then lead to the increase of noise when the motor is running.
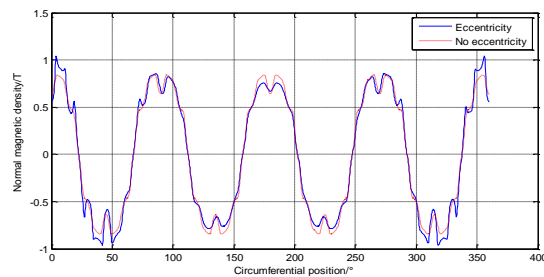

(a) Normal component
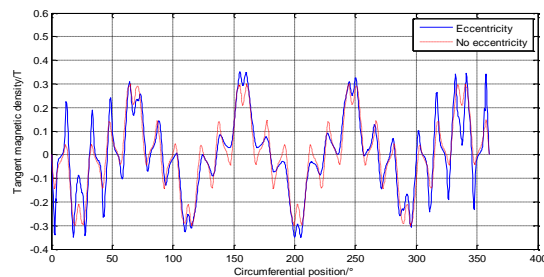
(b) Tangential component

Fig. 8: Air-gap magnetic density

A constant-speed driving mode is adopted in 2-D FE model to keep the straight prototype rotating at a constant speed. In view of the analogical change laws found in the EMF of all 12 winding elements, only the elements A1, A2, A3 and A4 of A-phase winding are analyzed as examples. Fig. 9(a) shows the EMF of elements after the straight prototype makes one revolution. The axial positions of A1 and A4 are close to the direction in which the air-gap thickness becomes thinner, and the air-gap magnetic density near them increases. Therefore, the EMF of A1 and A4 under the eccentric fault condition are higher than those under

completely healthy condition. On the contrary, the axial positions of A2 and A3 are close to the direction in which the air-gap thickness becomes thicker, and the air-gap magnetic density near them decreases. Therefore, the EMF of A2 and A3 under the eccentric fault condition are lower than those under completely healthy condition.

The EMF of four winding elements can be superimposed to synthesize the EMF of one phase winding. Since the EMF waveforms of the three-phase windings are similar, only the A-phase winding is analyzed as an example, as shown in Figure 9(b). It can be seen that the EMF waveform under eccentric fault condition almost coincides with that under completely healthy condition and the rotor static eccentricity has a weak influence on the EMF of winding phase. The reason is that the increase and decrease of EMF of winding elements are basically offset, and the sum is almost unchanged.
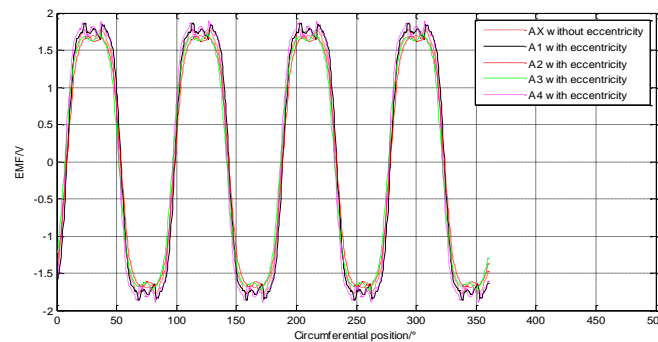
(a) Winding elements
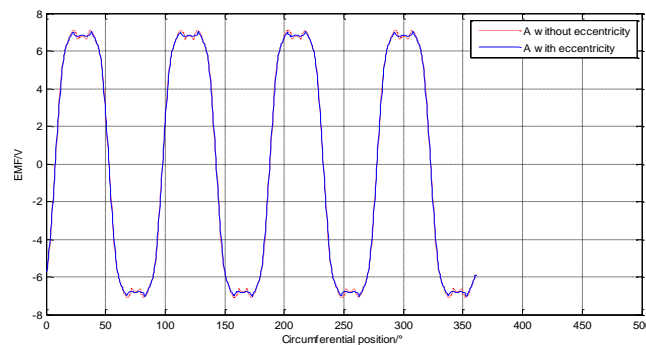
(b) Phase winding

Fig. 9: EMF of straight prototype

One revolution is taken as a cycle and the harmonic analysis of the EMF of A-phase winding is carried out. In view of the extremely small amplitude of higher harmonic components, only harmonic data within 100 orders are listed in Fig. 10. It can be seen that the harmonic components under the eccentric fault condition are similar to those under completely healthy conditions. The EMF is mainly composed of 4th, 12th and 20th harmonic components, and the proportion of other harmonic components is very small. No new harmonic components are introduced by the eccentricity fault, and the periodicity of EMF is not changed.
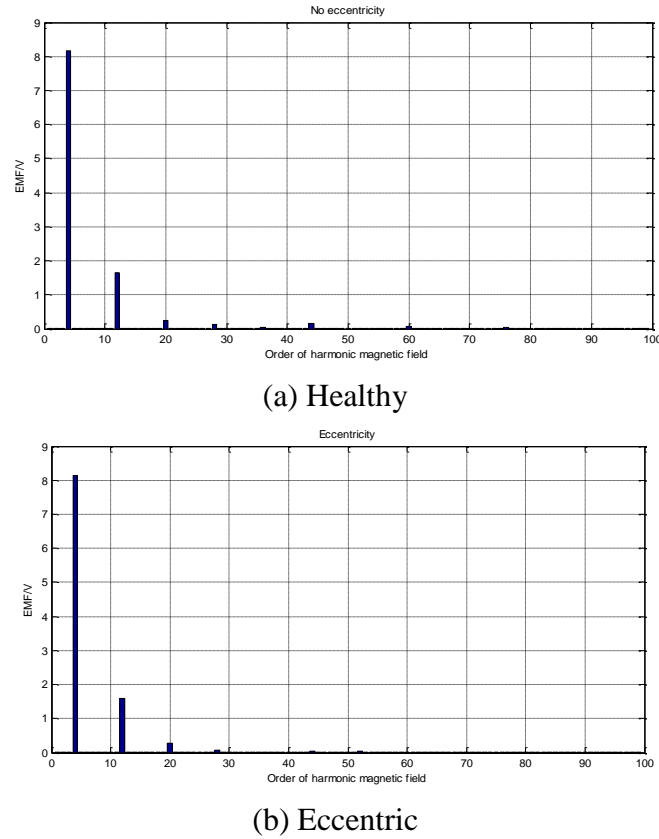
(a) Healthy

(b) Eccentric

Fig. 10: Harmonic components of EMF of straight prototype

If the motor rotates one revolution, it can be seen from the above 2-D magnetic field analysis results that four complete periods of EMF waveforms can be obtained. In the next research content of this paper, only one period of EMF is analyzed. According to the designed rules, the EMF of skewed prototype can be obtained by superimposing the results of 2-D magnetic field analysis. A complete period of EMF waveform of A-phase winding is shown in Fig. 11(a). It can be seen that even if a serious static eccentricity fault occurs, the influence is not obvious. A quarter of one revolution is taken as the period and the harmonic analysis is carried out. Harmonic analysis results are shown in Fig. 11(b). It can be seen that the rotor static eccentricity fault only slightly weakens the amplitude of low-order harmonic components, and has little effect on high-order harmonic components.
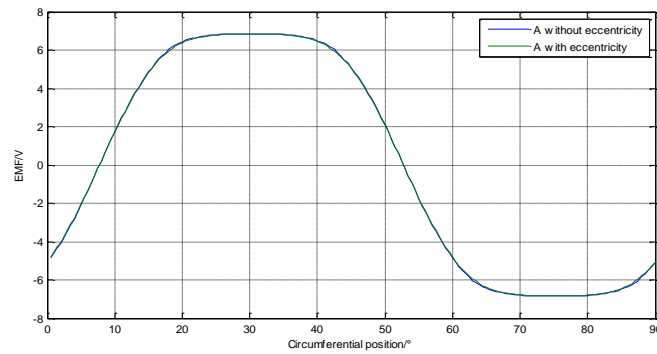
(a) Waveforms
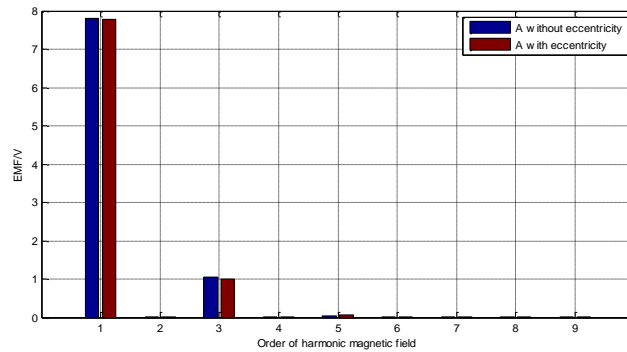
(b) Harmonic components

Fig. 11: EMF of one cycle of skewed prototype

By comparing the waveforms in Fig. 9(b) and Fig. 11(a), it can be seen that the stator skewed structure can effectively change the unsmooth EMF waveform into a smooth flat-top waveform regardless of whether the rotor is static eccentric. By comparing the data in Fig. 10 and Fig. 11(b), it can be seen that the stator skewed structure can effectively weaken the higher harmonic components of EMF, but has little effect on the lower harmonic components.

Taking the whole air-gap circumferential path as one cycle, the harmonic analysis of air-gap normal magnetic density data series is carried out in Fig. 12. In view of the extremely small amplitude of high harmonic components, only components within 99 orders are listed. It can be seen from Fig. 12(a) that if the motor is healthy, the air-gap magnetic density only contains harmonic components of multiples of 4. The air-gap magnetic density is mainly composed of low-order harmonic components, while the amplitude of high-order harmonic components is extremely small. This means that the calculation accuracy of multi-slice model is higher for solving healthy skewed prototype. Comparing Fig. 12(a) with Fig. 12(b), it can be seen that the static eccentricity of rotor has obvious influence on the periodicity of air-gap magnetic density. A large number of low-order harmonic components and high-order harmonic components are introduced, but the amplitude of these introduced harmonic components is relatively small. This means that, although the calculation accuracy of the multi-slice model for solving the eccentric skewed prototype is lower than that of the healthy skewed prototype, it also meets the general engineering needs.
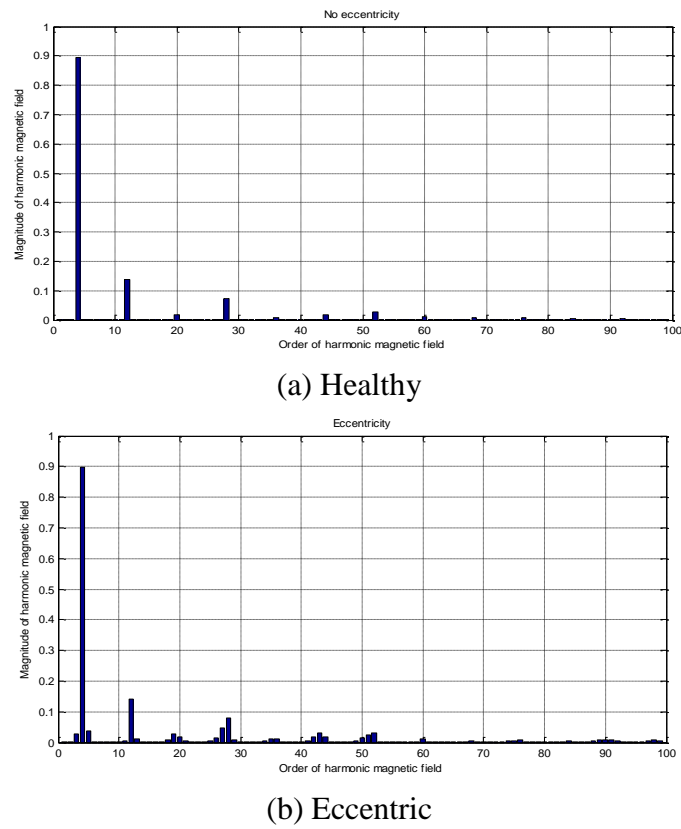
(a) Healthy

(b) Eccentric

Fig. 12: Harmonic components of magnetic density

Prototypes were manufactured according to the design scheme. The photos are shown in Fig. 13 and three of them are selected randomly. Driving performances of forward and reverse rotations are tested at room temperature.

The resistance test data shown in Fig. 14(a) and inductance test data shown in Fig. 14(b) have little difference. The six curves in Fig. 14(c) show the relationship between bus current and rotating speed. The six curves in Fig. 14(d) show the relationship between bus current and output torque. The curves are almost coincident. The above data show that this batch of test prototypes have high machining accuracy and good consistency.
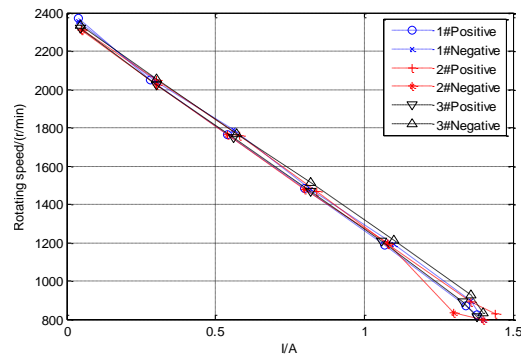
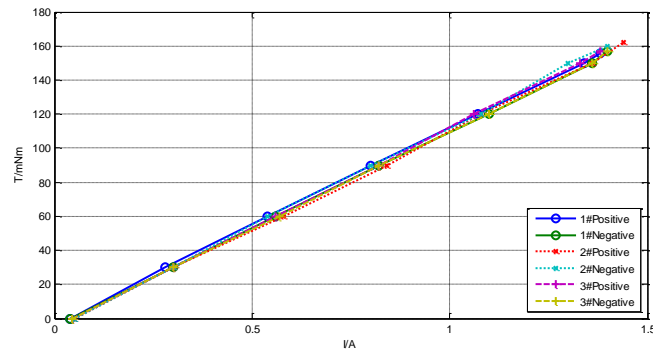

Fig. 13: Photos of tested prototypes
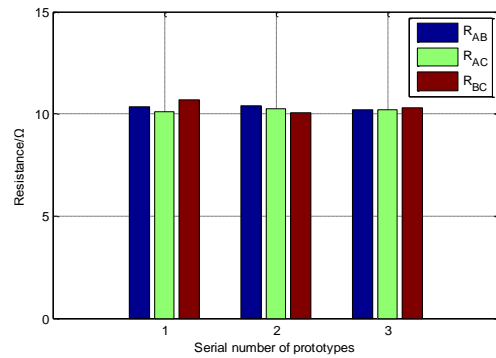
(a) Resistance
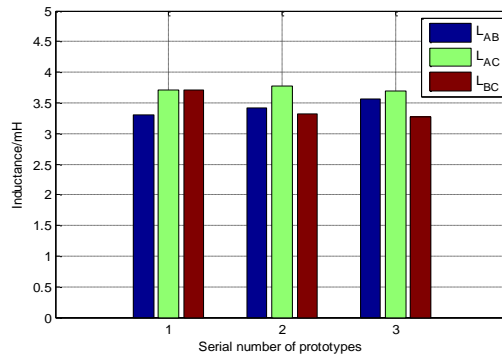
(b) Inductance

(c) Relationship between bus current and rotating speed

(d) Relationship between bus current and output torque

Fig. 14: Test data of prototypes

Fig. 15 shows the comparison between the prototype performance calculated by the simplified model and the average value of the prototype physical test results. The comparison results prove the effectiveness of the proposed modeling method.

The comparison between the calculated data and test data of the multi-slice model with 20 slices is shown in Fig. 15. In the figure, the blue solid line refers to the calculated data of the multi- slice model, while the green dotted line refers to the average value of the six measured curves. It is difficult to establish an accurate mathematical model of friction torque. In order to ensure the objective and reliable calculation data, the friction correlation coefficient is set to zero in 2-D FE modeling. Therefore, the torque calculated by the multi- slice model refers to the electromagnetic torque. The torque obtained by prototype test refers to the output torque. Because of the existence of friction torque, when the output torque is zero, the no-load current is not zero. The prototype is not a high-speed motor. The rated speed is 1350 r/min, and the ideal no-load speed is around 2400 r/min. Then, the friction torque can be approximately considered as a constant, and the current-output torque curve can be obtained by translating the current-electromagnetic torque curve. In this way, it is convenient to compare with the prototype test data.

By comparing the data in the figure, it can be known that the torque constant calculated by the multi-slice model is close to the torque constant obtained by the test. At the rated current of 1.2A, the output torque calculated by the multi-slice model is 0.136 Nm, which is only 0.018 Nm higher than the measured value, and the relative error is less than 16%. Therefore, the multi-slice model can meet the precision requirements of general engineering.
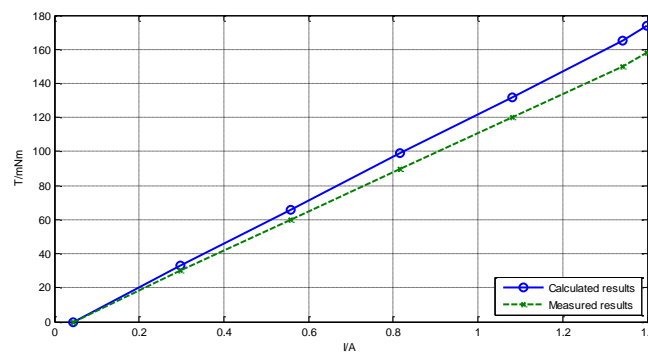

Fig. 15: Comparison between calculated data and test data

V. CONCLUSION

This paper proposed a simplified modeling method, which can synthesize 3-D field calculation results from 2-D electromagnetic field analysis data. The simplified model of rare-earth permanent magnet brushless DC motors with static rotor eccentricity and skewed stator slots was established. The effects of static rotor eccentricity on the magnetic field distribution and winding EMF were investigated.

The research results indicated that rotor static eccentricity will significantly affect the magnetic field distribution, but has little effect on EMF. The prototype test results prove the effectiveness of the proposed simplified modeling method.

The multi-slice model has the advantages of rapidity and relative accuracy for calculating the skewed motor, but there are still some points worthy of further study in this algorithm. First of all, the multi-slice model is based on the 2-D FEM, and it is inevitable to ignore the end-region magnetic field of motors. So, it is necessary to study the compensation method of end magnetic leakage. Secondly, the winding current of the straight motor is axial, while the actual winding current of the skewed motor has transverse component as well as axial component. It is necessary to study the influence of the transverse component of current neglected by the multi-slice model on the calculation results and its compensation method.

REFERENCES

[1] S. B. Santra, A. Chatterjee, D. Chatterjee, S. Padmanaban and K. Bhattacharya, "High Efficiency Operation of Brushless DC Motor Drive Using Optimized Harmonic Minimization Based Switching Technique," in IEEE Transactions on Industry Applications, vol. 58, no. 2, pp. 2122-2133, March-April 2022, doi: 10.1109/TIA.2022.3146212.

[2] J. Cai, X. Zhang, W. Zhang and Y. Zeng, "An Integrated Power Converter-Based Brushless DC Motor Drive System," in IEEE Transactions on Power Electronics, vol. 37, no. 7, pp. 8322-8332, July 2022, doi: 10.1109/TPEL.2022.3144897.

[3] S. Singh, N. B. Y. Gorla, K. Jayaraman and J. Pou, "Analysis and Mitigation of the Common-Mode Noise in a Three-Phase SiC-Based Brushless DC Motor Drive With 120° Conduction Mode," in IEEE Transactions on Power Electronics, vol. 37, no. 5, pp. 5514-5523, May 2022, doi: 10.1109/TPEL.2021.3133880.

[4] M. Ebadpour, N. Amiri and J. Jatskevich, "Fast Fault-Tolerant Control for Improved Dynamic Performance of Hall-Sensor-Controlled Brushless DC Motor Drives," in IEEE Transactions on Power Electronics, vol. 36, no. 12, pp. 14051-14061, Dec. 2021, doi: 10.1109/TPEL.2021.3084921.

[5] A. Sen and B. Singh, "Peak Current Detection Starting Based Position Sensorless Control of BLDC Motor Drive for PV Array Fed Irrigation Pump," in IEEE Transactions on Industry Applications, vol. 57, no. 3, pp. 2569-2577, May-June 2021, doi: 10.1109/TIA.2021.3066831.

[6] S. Wu, T. Shi, Z. Chen, L. Guo, Z. Wang and Z. Song, "Analytical Modeling of Equivalent Air-Gap Length and Inductance Calculation of Interior Permanent Magnet Motors," in IEEE Transactions on Magnetics, vol. 58, no. 2, pp. 1-11, Feb. 2022, Art no. 8104011, doi: 10.1109/TMAG.2021.3131526.

[7] Y. Wang, K. Liu, W. Hua, C. Zhang, Z. Wu and H. Zhang, "Analysis and Detection of Rotor Eccentricity in Permanent Magnet Synchronous Machines Based on Linear Hall Sensors," in IEEE Transactions on Power Electronics, vol. 37, no. 4, pp. 4719-4729, April 2022, doi: 10.1109/TPEL.2021.3131576.

[8] W. Deng, S. Zuo, W. Chen, Z. Qian, C. Qian and W. Cao, "Comparison of Eccentricity Impact on Electromagnetic Forces in Internal- and External-Rotor Permanent Magnet Synchronous Motors," in IEEE Transactions on Transportation Electrification, vol. 8, no. 1, pp. 1242-1254, March 2022, doi: 10.1109/TTE.2021.3112521.

[9] J. Ren, X. Wang and W. Zhao, "Magnetic Field Prediction of the Saturated Surface-Mounted Permanent Magnet Synchronous Machine With Rotor Eccentricity," in IEEE Transactions on Industrial Electronics, vol. 69, no. 8, pp. 7756-7766, Aug. 2022, doi: 10.1109/TIE.2021.3105985.

[10] T. R. He, Z. Q. Zhu, F. Xu, Y. Wang, H. Bin and L. M. Gong, "Influence of Rotor Eccentricity On Electromagnetic Performance of 2-pole/3-slot PM Motors," in IEEE Transactions on Energy Conversion, vol. 37, no. 1, pp. 696-706, March 2022, doi: 10.1109/TEC.2021.3098669.

[11] M. S. Rafaq et al., "Airgap Search Coil Based Identification of PM Synchronous Motor Defects," in IEEE Transactions on Industrial Electronics, vol. 69, no. 7, pp. 6551-6560, July 2022, doi: 10.1109/TIE.2021.3095810.

[12] Y. -L. He et al., "A Novel Universal Model Considering SAGE for MFD-Based Faulty Property Analysis Under RISC in Synchronous Generators," in IEEE Transactions on Industrial Electronics, vol. 69, no. 7, pp. 7415-7427, July 2022, doi: 10.1109/TIE.2021.3094481.

[13] T. -K. Bang, K. -H. Shin, J. -I. Lee, H. -K. Lee, H. -W. Cho and J. -Y. Choi, "Electro-Mechanical Characteristics Analysis and Experimental Study of PMSM According to Rotor Eccentricity," in IEEE Transactions on Magnetics, vol. 58, no. 2, pp. 1-5, Feb. 2022, Art no. 8103205, doi: 10.1109/TMAG.2021.3092575.

[14] M. F. Shaikh, H. -j. Kim, S. B. Lee and C. Lim, "Online Airgap Flux Based Diagnosis of Rotor Eccentricity and Field Winding Turn Insulation Faults in Synchronous Generators," in IEEE Transactions on Energy Conversion, vol. 37, no. 1, pp. 359-366, March 2022, doi: 10.1109/TEC.2021.3092198.

[15] Z. Yang, C. Sun, X. Sun and Y. Sun, "An Improved Dynamic Model for Bearingless Induction Motor Considering Rotor Eccentricity and Load Change," in IEEE Transactions on Industrial Electronics, vol. 69, no. 4, pp. 3439-3448, April 2022, doi: 10.1109/TIE.2021.3071712.

[16] Z. Masoumi, B. Moaveni, S. M. M. Gazafrudi and J. Faiz, "Online Model-Based Fault Detection of Synchronous Generators Using Residual Analysis," in IEEE Access, vol. 9, pp. 163697-163706, 2021, doi: 10.1109/ACCESS.2021.3133368.

[17] H. De Gersem and L. A. M. D'Angelo, "Modeling Skew by Single- and Multi-Slice 2-D Machine Models," in IEEE Transactions on Magnetics, vol. 57, no. 6, pp. 1-4, June 2021, Art no. 8105404, doi: 10.1109/TMAG.2021.3065901.

[18] A. Marfoli, L. Papini, P. Bolognesi and C. Gerada, "An Analytical-Numerical Approach to Model and Analyse Squirrel Cage Induction Motors," in IEEE Transactions on Energy Conversion, vol. 36, no. 1, pp. 421-430, March 2021, doi: 10.1109/TEC.2020.3007385.

[19] T. Liu, M. Jiang, D. Zhang, H. Zhao and F. Shuang, "Effect of Symmetrical Voltage Sag on Induction Motor Considering Phase-Angle Factors Based on a New 2-D Multi-Slice Time-Stepping Finite Element Method," in IEEE Access, vol. 8, pp. 75946-75956, 2020, doi: 10.1109/ACCESS.2020.2988581.

[20] C. Hong, W. Huang and Z. Hu, "Performance Calculation of a Dual Stator Solid Rotor Axial Flux Induction Motor Using the Multi-Slice and Multi-Layer Method," in IEEE Transactions on Magnetics, vol. 55, no. 2, pp. 1-9, Feb. 2019, Art no. 8100709, doi: 10.1109/TMAG.2018.2872457.

[21] D. Zhang, T. Liu, C. He and T. Wu, "A New 2-D Multi-Slice Time-Stepping Finite Element Method and Its Application in Analyzing the Transient Characteristics of Induction Motors Under Symmetrical Sag Conditions," in IEEE Access, vol. 6, pp. 47036-47046, 2018, doi: 10.1109/ACCESS.2018.2867277.

[22] J. Keränen, P. Ponomarev, J. Pippuri, P. Råback, M. Lyly and J. Westerlund, "Parallel Performance of Multi-Slice Finite-Element Modeling of Skewed Electrical Machines," in IEEE Transactions on Magnetics, vol. 53, no. 6, pp. 1-4, June 2017, Art no. 7201204, doi: 10.1109/TMAG.2017.2653421.

[23] C. Xia, Z. Zhang and Q. Geng, "Analytical Modeling and Analysis of Surface Mounted Permanent Magnet Machines With Skewed Slots," in IEEE Transactions on Magnetics, vol. 51, no. 5, pp. 1-8, May 2015, Art no. 8104508, doi: 10.1109/TMAG.2014.2364156.